Vortex-core properties and vortex-lattice transformation in FeSe

A. V. Putilov, C. Di Giorgio, V. L. Vadimov, D. J. Trainer, E. M. Lechner, J. L. Curtis, M. Abdel-Hafiez, O. S. Volkova, A. N. Vasiliev, D. A. Chareev, G. Karapetrov, A. E. Koshelev, A. Yu. Aladyshkin, A. S. Mel'nikov, and M. Iavarone

Phys. Rev. B **99**, 144514 — Published 16 April 2019

DOI: 10.1103/PhysRevB.99.144514

Vortex Core Properties and Vortex Lattice Transformation in FeSe

A. V. Putilov,[1,*] C. Di Giorgio,[1,†] V. L. Vadimov,[2] D. J. Trainer,[1] E. M. Lechner,[1] J. L. Curtis,[3] M. Abdel-Hafiez,[4,5,6] O. S. Volkova,[7,8,6] A. N. Vasiliev,[7,6,9] D. A. Chareev,[10,8,11] G. Karapetrov,[3] A. E. Koshelev,[12] A. Yu. Aladyshkin,[2,1] A. S. Mel'nikov,[2] and M. Iavarone[1]

[1]*Department of Physics, Temple University, Philadelphia, Pennsylvania 19122, USA*
[2]*Institute for Physics of Microstructures RAS, Nizhny Novgorod, GSP-105, Russia 603950*
[3]*Department of Physics, Drexel University, Philadelphia, Pennsylvania 19104, USA*
[4]*Center for High Pressure Science and Technology Advanced Research, Shanghai, 201203, China*
[5]*Fayoum University, Fayoum 63514, Egypt*
[6]*National University of Science and Technology "MISiS", Moscow 119049, Russia*
[7]*Physics Faculty, M.V. Lomonosov Moscow State University, Moscow 119991, Russia*
[8]*Ural Federal University, 620002 Ekaterinburg, Russia*
[9]*National Research South Ural State University, Chelyabinsk 454080, Russia*
[10]*Institute of Experimental Mineralogy, Russian Academy of Sciences, 142432 Chernogolovka, Moscow District, Russia*
[11]*Kazan Federal University, Kazan 420008, Russia*
[12]*Materials Science Division, Argonne National Labratory, Argonne, IL 60439, USA*

(Dated: March 25, 2019)

Low-temperature scanning tunneling microscopy and spectroscopy has been used to image the vortex core and the vortex lattice in FeSe single crystals. The local tunneling spectra acquired at the center of elliptical vortex cores display a strong particle-hole asymmetry with spatial oscillation, characteristic of the quantum-limit vortex core. Furthermore, a quasi-hexagonal vortex lattice at low magnetic field undergoes noticeable rhombic distortions above a certain field ~ 1.5 T. This field H^* also reveals itself as a kink in the magnetic field dependence of the specific heat. The observation of a nearly hexagonal vortex lattice at low field is very surprising for a materials with an orthorhombic crystal structure and it is in apparent contradiction with the elliptical shape of the vortex cores. These observations can be directly connected to the multiband nature of superconductivity in this material, provided we attribute them to the suppression of superconducting order parameter in one of the energy bands. Above the field H^* the superconducting coherence length for this band can well exceed the intervortex distance which strengthens the nonlocal effects. Therefore, in addition to multiple-band effects, other possible sources that can contribute to the observed evolution of the vortex-lattice structure include nonlocal effects which cause the field-dependent interplay between the symmetry of the crystal and vortex lattice or the magneto-elastic interactions due to the strain field generated by vortices.

I. I. INTRODUCTION

Vortices in superconductors reveal in different ways important aspects of the normal and superconducting state properties. The spatial distributions of the quasiparticle density of states in a vortex core depend on the specific Fermi surface, gap anisotropy and symmetry of the superconducting order parameter[1,2], and they are observable only in the case of clean limit $\xi < l$ (where ξ is the coherence length of the superconductor and l is the mean-free path), otherwise they can be suppressed by the quasiparticle scattering. A broad variety of vortex-core shapes has been observed in different clean superconducting materials. In 2H-$NbSe_2$ a six-fold symmetrical shape of vortices has been reported [3,4], a four-fold symmetry has been observed in YNi_2B_2C [5,6] while striped vortex core states which are largely influenced by patches of different short-range order have been observed in $Bi_2Sr_2CaCu_2O_{8+x}$ [7]. Recently, vortices were also observed in the heavy-fermion superconductor $CeCoIn_5$ [8,9]. The core shows bound states located at zero bias, which have an in-plane four-fold anisotropy and an asymmetric spatial dependence [8]. This four-fold core symmetry has a strong relation to the anisotropic gap structures found in macroscopic measurements [10]. An elongated two-fold vortex core has been observed in FeSe films [11] and single crystals [12] and it has been explained in terms of the nematicity of the system [13,14].

Besides investigations of the vortex cores, the way the symmetry of the vortex lattice is shaped by the materials' properties has also been studied intensively using different vortex imaging techniques. In isotropic superconductors vortices form a hexagonal vortex lattice (in absence of pinning) [15,16]. However, square vortex lattices have been also reported in many materials [17,18]. Indeed, the difference in the free energy for the hexagonal and the square vortex lattice is found to be only 2% [16]. Therefore, a weak anisotropy can change the balance and lead to a distorted hexagonal or square vortex lattice. Many theoretical papers have addressed the role of the symmetry of the superconducting order parameter and the influence on the vortex lattice structure and they consistently found that a square vortex lattice can be stabilized when the applied magnetic field is increased in the case of d-wave symmetry. [19–21]. On the other hand, the Fermi surface anisotropy combined with nonlocal electrodynamics can be also responsible for vortex lattice transitions. Theoretically, the corresponding nonlocal corrections to

the London model have been used to calculate the vortex lattice free energy and determine the stable vortex configurations as a function of magnetic field [22–24]. Recently a vortex lattice transition from hexagonal to a distorted tetragonal has also been reported for $CsFe_2As_2$ that has been explained considering the intervortex interactions and the crystal structure[25]. Other investigated structural properties of vortex lattices include distorted hexagonal symmetry, vortex chains [26], order-disorder transitions[27], pinning by twin boundaries[28].

Among the Fe-based superconductors, FeSe has attracted a lot of attention because the tetragonal-to-orthorhombic structural transition is not accompanied by an ordered magnetic state in the whole temperature range down to the superconducting transition (in contrast to other Fe-based superconductors). Therefore, the nematic state that sets in below the structural transition and manifests itself in many electronic properties, persists also in the superconducting state[29]. The microscopic origin of this nematic state is still extensively debated. The key issue is whether this state is mostly driven by spin or orbital fluctuations[29]. Also, it is not clear if there is any link between the nematic and superconducting orders. The Fermi surface consists of multiple bands, with a hole pocket at the Γ point and electron-like pockets at the Brillouin zone corners[30–35].

In the following, we report low-temperature scanning tunneling microscopy and spectroscopy (STM/STS) experiments showing an anisotropic vortex core in the quantum limit and a noticeable vortex lattice transformation. We discuss these results in the context of the existing theories and the anisotropic multiband nature of the superconductivity in this material.

STM/STS measurements provide a unique possibility for directly probing both the changes in the structure of the vortex lattice and the shape of individual vortex cores. When STM/STS results are complemented by thermodynamic measurements, the distinctive features of the vortex matter can provide us a deeper insight into the physics of superconducting correlations.

For the particular case of FeSe our experimental data contain three important observations: (i) we find a characteristic magnetic field $H^* \sim 1$T separating the low-field regime with an almost hexagonal vortex lattice and high-field regime with gradually increasing orthorhombic distortions in the vortex lattice structure; (ii) The crossover at the field close to the H^* value reveals itself on the field dependence of the specific heat (see Fig.4b) where we clearly observe a change of the slope in the magnetic field interval 1 T $< H <$ 2 T. (iii) Our observation of a nearly hexagonal vortex lattice at low magnetic fields is a surprising result for an orthorhombic material which is also in apparent contradiction with the elliptical shape of vortex cores.

The paper is organized as follows. In Sec. II, we briefly discuss some experimental details of our samples and approaches. In the main Sec. III, we present the results of our experimental findings as well as the discussion and a simple theoretical model describing the behavior of the vortex lattice distortions. Finally, the results are summarized in Sec. IV.

II. II. EXPERIMENTAL DETAILS

FeSe single crystals were grown in evacuated quartz ampoules using the AlCl3/KCl flux technique in a temperature gradient (from 400°C to ∼350°C) for 45 days[36]. The chemical composition of crystals was studied with a digital scanning electron microscope TESCAN Vega II XMU[36].

The crystals have a plate-like shape with the c-axis oriented perpendicular to the crystal plane with only the tetragonal β-FeSe phase present. The lattice parameters $c = (5.52 \pm 0.01)\mathring{A}$ and $a = (3.77 \pm 0.01)\mathring{A}$ were found via X-ray diffraction for FeSe single crystals.

Low-temperature scanning tunneling microscopy and spectroscopy have been performed at $T = 1.5$K using Unisoku UHV STM system, with a base pressure of 4×10^{-11} Torr. The samples were cleaved in UHV at room temperature and soon after were transferred to the STM at low temperature. Pt-Ir tips were used in all of our experiments, therefore the tunneling conductance between a normal electrode (tip) and a sample provides, in the limit of low voltages, the local quasiparticle density of states of the sample. Tunneling spectroscopy was performed using a standard lock-in technique with an ac modulation of 0.2 mV at 373 Hz. The vortex lattice is visualized by acquiring the lock-in signal (conductance) maps at $E = E_F$ while scanning the tip over the sample surface at higher voltage (20 mV) at each location. Topography was always acquired simultaneously to assure the location where the spectroscopic information was recorded.

Low-temperature specific heat data were obtained under the applied field from 0 to 9 T using the Quantum Design physical property measurement system (PPMS) via the relaxation method.

III. III. RESULTS AND DISCUSSION

A. A. VORTEX CORE

Scanning tunneling microscopy measurements of FeSe single crystals (with a superconducting critical temperature of ∼ 9K) reveal atomically flat surfaces. Figure 1(a) shows an atomic resolution topographic image of the surface of FeSe at $T = 1.5$K (topmost Se layer). The image also shows the presence of dimer-like defects (bright spots) surrounded by dark regions that are usually associated with Fe vacancies[37]. They are aligned both along the a- and b-axis, which point to their independence from a structural orthorhombic distortion[38]. The inset of Figure 1(a) shows a zoom-in image of the Se lattice and reveals a regular square lattice of the topmost Se atoms

with a lattice parameter of $a = 3.77\mathring{A}$, consistent with X-ray investigation. The small difference of the in-plane lattice parameters that sets in at the structural transition is below 1% and below the STM resolution.

Differential tunneling conductance spectra $dI/dV(\vec{r}, E)$ recorded as a function of the sample-tip voltage V, are proportional to the local density of states (LDOS), $N(\vec{r}, E)$. In multiple-band materials, partial densities of states of different bands contribute to the tunneling conductance with different weights. When a magnetic field is applied along the c-axis of the crystal, Abrikosov vortices enter the sample and modify the local density of states. Vortices can be imaged by STM by mapping the local conductance at an energy where a vortex alters the density of states. Therefore, STM is a direct experimental technique to visualize vortices in superconductors with high spatial resolution.

Figure 1(b) shows a map of the zero bias conductance (ZBC) representing the LDOS at the Fermi level, of the same scan area as in Figure 1(a). The image shows a single vortex core elongated in one of the Fe-Fe bond directions (at 45 degrees with the Se topmost lattice).

General theoretical models accounting for the vortex shape include superconducting gap anisotropy [39,40] as well as Fermi surface anisotropy [41–43]. The competing effects between these two factors in the optimal vortex lattice structure for fourfold symmetric superconductors are discussed in Ref.[44]. In general, the spatial decay of the vortex core states happens on the length scale of $\xi_{BCS} = \hbar v_F/\pi\Delta$, where $\hbar$ is the reduced Planck constant, v_F is the Fermi velocity and Δ is the gap amplitude. Therefore, in the case of an anisotropic gap where $\Delta(\mathbf{k}) \neq$ const, the vortex shape in real space is directly influenced by this anisotropy and, in particular, the vortex extends in the directions of gap minima or nodes. However, the directional dependence of $v_F(\mathbf{k})$ also affects the vortex core shape, and in the case of Fe-based superconductors in absence of strong nodes the Fermi velocity anisotropy can determine the anisotropy of the decay length of vortex core states[45].

STM can be used to probe the electronic states within the vortex core directly. The spatial evolutions of the tunnelling spectra along the long and short axis of the elliptical vortex core are reported in the intensity plot of $N(\vec{r}, E)$ in Figure 1(c) and (d). Individual spectra taken at representative points are depicted in Figure 1(e) and (f).

In clean superconductors, at the vortex core the tunneling conductance should show low-energy excitations predicted by Caroli, de Gennes, and Matricon (CdGM)[46] due to the electron confinement. In conventional superconductors, due to the very small value of the ratio Δ/E_F (where Δ is the superconducting gap and E_F is the Fermi energy), these discrete energy levels appear as a broad symmetric peak at E_F. Usually, away from the center the zero-bias peak splits into two peaks symmetric in energy[3,4]. If the temperature is low enough, such that the quantum limit $T/T_c < \Delta/E_F$ is satisfied, low energy excitations at $E_n = (n+1/2)\Delta^2/E_F$ $(n = 0, 1, 2\ldots)$ should become detectable in very clean materials. However, usually the quantum limit is reached in conventional superconductors at very low temperature (in $NbSe_2$ for example at $T < 50$ mK). CdGM states for the quantum limit have been argued for YNi_2B_2C[6], $Bi_2Sr_2CaCu_2O_{8+\delta}$[47], $YBa_2Cu_3O_{7-\delta}$[48] and, more recently, in some Fe-based superconductors[49–52].

In the case of FeSe, the evolution of the local density of states along the shorter direction is smooth (see Figure 1(d)) with low-energy peaks that evolve spatially and converge into the coherence peak. On the contrary, there appears an oscillatory behavior along the longer direction, where the intensities of vortex bound states oscillate in space and it is particle-hole asymmetric, i.e., the differential conductance intensity of the bound state peak on negative energy is larger than that on positive energy (see Figure 1(c)). Such asymmetry appears in the so-called 'quantum-limit' vortex bound state[53]. The energy of the bound state along the longer direction is at $E_{n=0} = 0.55$ mV and almost does not shift when the STM tip moves away from vortex center as it is shown in Figure 1(e). This yields a value of $E_F \approx 5$ meV and a ratio $\Delta/E_F \approx 0.5$ (where $\Delta = 2.35$ meV) consistent with other estimates[33,54]. This small value of E_F confirms that this material is in the quantum limit.

To extract the coherence lengths from the maps, we fit the spatial dependence of the zero-bias conductance in the vortex core with an exponential decay of the form $G(x, y) = G_\infty + A\sum_i \exp\left(-\sqrt{\frac{(x-x_i)^2}{\xi^2_{Long}} + \frac{(y-y_i)^2}{\xi^2_{Short}}}\right)$. Here G_∞ is the conductance value in between the vortex cores and the summation is performed over the first neighbors. Keeping the neighboring vortices in the summation improves the fit for the maps at high magnetic fields when the vortices overlap. In the trivial case of a single-band superconductor and an isotropic matrix element describing the tunneling from the STM tip to the surface, we would expect that the lengths ξ_{Long} and ξ_{Short} can be considered as the coherence lengths along different directions.

We find that $\xi_{Short} \propto 1/\sqrt{H} + const$, as expected for a superconductor in the clean limit in large fields[55,56] while $\xi_{Long} \approx const$. The extracted magnetic field dependences of ξ_{Long} and ξ_{Short} are shown in Figure 2(a). The absolute values of the low-field coherence lengths are consistent with the value $\xi_{ab}^{H_{c2}} \approx 4.4$nm, which can be extracted from the low-temperature upper critical field ~ 17 T[54]. Figure 2(b) reports the anisotropy of the coherence lengths that increases as the magnetic field increases. The spatial dependence of the zero-bias conductance along the two high-symmetry direction of the vortex is shown in Figure 2(c) and (d) for the vortices in the 2T image.

Quantitatively, the gap anisotropy for the Γ band reported in [57] is very large $\Delta_{\max}/\Delta_{\min} \sim 15$. If one assumes that the contribution of the tunneling current from the Γ band dominates in the STM signal and the

anisotropy of the vortex core reflects properties of this band, the gap anisotropy in the Γ band ∼ 15 should be partially compensated by the v_F anisotropy ∼ 1.5[57]. Still this compensation can not provide the moderate anisotropy of the vortex core shape ∼ 1.5 − 2.5 observed in Figure 2(b). This implies that the tunneling from the electron pocket should be also taken into account. Indeed, the gap anisotropy in the electron ε pocket is opposite to the Γ pocket[57]. Therefore, the magnetic field dependence anisotropy of the vortex core seems to reflect the multiband character of this material.

STM observation of the field dependence of the coherence length has been reported in the single-band superconductor β-Bi_2Pd[58] and in the two-gap superconductors $NbSe_2$[59] and $CaKFe_4As_4$[60], whereas a magnetic field independent coherence length has been observed in multigap materials in the dirty limit such as 2H-$NbSe_{1.8}S_{0.2}$ and 2H-NbS_2[58].

B. B. VORTEX LATTICE TRANSFORMATION

We used the STM conductance maps to visualize the vortex lattice in this compound and found that its structure evolves with the applied magnetic field. A set of differential conductance images for four applied magnetic fields between 1T and 6T applied perpendicular to the a-b plane of the sample is shown in Figs. 3(a)-(d). In order to analyze the vortex structure, we performed Delaunay triangulation of the real-space images, as summarized in Figs. 3(e)-(h). In this analysis each vertex denotes the position of a vortex. Figs. 3(i)-(l) shows the Fourier transform of the conductance maps showing an almost hexagonal vortex lattice at low fields that transforms in a rhombic lattice and then in a nearly square lattice as the magnetic field is increased and the vortices move closer together. The vortices interact with each other through the circulating currents around each vortex and form a lattice in equilibrium.

At small distances from the core, the current pattern reflects the symmetry of the electronic states and may give rise to a complex evolution of vortex lattice structures with applied field[44]. In the case of the nonmagnetic borocarbides and A15 materials, the vortex lattice transition observed have been explained in terms of nonlocality, i. e. the property of clean superconductors that the current density at any position **r** is determined by the vector potential within a region of radius ξ around this position. As the connection between the current density and the vector potential depends on the shape of Fermi surface, this shape will be reflected in the vortex-vortex interaction and ultimately in the structure of the vortex lattice. The analysis of these images is summarized in Figure 4(a), where the average angle obtained from the Delaunay triangulation is plotted as a function of the applied magnetic field. An almost hexagonal lattice is obtained at low field characterized by a unimodal distribution of angles centered at about 60°, shown in Figure 4(c). The probability distribution function with three maxima at 45°, 60° and 80° is instead observed in the transition region, pointing to a co-existence of hexagonal and rhombic lattices in the same scanning area (Figure 4(d)). At high fields a bimodal distribution with two local maxima near 45° and 80° is observed as shown in Figure 4(e).

The magnetic-field dependence of specific heat is another excellent sensitive independent tool to probe the vortex excitations in a mixed state. At low temperatures, the specific heat in finite magnetic field usually has linear temperature dependence, $C(H,T) \propto \gamma(H)T$. For the isotropic *s*-wave order parameter the coefficient γ is proportional to the magnetic field, $\gamma(H) \propto H$ because the specific heat in the vortex state is dominated by the contribution from the localized quasiparticles in the vortex cores. On the other hand, for a superconductor with nodes in the gap, for example *d*-wave superconductors with line nodes, Volovik et al.[62] pointed out that the Doppler shifts in the quasiparticle spectrum due supercurrents around a vortex core qualitatively modify the field dependence as $\gamma(H) \propto \sqrt{H}$.

The field dependence of the specific heat coefficient is presented in Figure 4(b). The data deviate from both the linear ($\gamma \propto H$) and square-root ($\gamma \propto \sqrt{H}$) behavior in agreement with other reports[63]. FeSe indeed is not a simple isotropic *s*-wave or nodal superconductor[12,57,64,65]. In the case of a two-band superconductor with strongly different gaps, $\gamma(H)$ increases steeply with the field caused by the suppression of the smaller gap by increasing magnetic field [66]. It is evident that the slope of $\gamma(H)$ at low field is larger than that at higher field, which has been observed also in two-gap superconductors such as MgB_2[66]) and $Lu_2Fe_3Si_5$ [67]. After the magnetic field exceeds H^*, the specific heat coefficient increases linearly with the applied field. Based on this, the typical field H^* is evaluated as 1 T corresponding to the kink in the data in Figure 4(b) and this value strongly correlates with the observed onset of the vortex lattice transformation in the STM data. We note that the value of γ at H^* is about $0.36\gamma_n$, where γ_n is the normal-state Sommerfield coefficient. Note that the residual value $\gamma_r = \gamma(H = 0)$ is determined by the zero-field density of subgap states which is presumably controlled by various types of defects and, thus, indicates the quality of the investigated single crystals.

C. C. DISCUSSION

To summarize, the key experimental observations which should be explained by an appropriate theoretical model can be listed as follows: (i) at low fields the vortex lattice anisotropy strongly differs from the anisotropy of the vortex core; (ii) the structure of the vortex lattice exhibits a crossover from an almost hexagonal one at low fields to the distorted square one at high fields; (iii) the core anisotropy grows with the increasing magnetic field;

(iv) the crossover in the magnetic field dependence of the heat capacity occurs at the field values close to the ones corresponding to the onset of the gradual change in the vortex lattice structure.

Naturally, an appropriate explanation of these experimental findings should be developed taking into account the previous results of the Refs.[30–32,68] indicating an essential two-band nature of superconducting state in FeSe. These observations include a noticeable difference between the gaps, Fermi velocities and, thus, the coherence lengths $\xi^{(1,2)}$ for the Cooper pair wavefunctions in different energy bands. Thus, the complicated structure of the superconducting order parameter reflecting the superconducting correlations at different bands is an obvious reason of possible changes in the structure of the vortex matter in this compound. The resulting multicomponent order parameter is well-known to be the cause of a variety of phase transitions and clustering in the vortex matter[69,70] as well as the gradual changes in the vortex lattice geometry[71].

As at low magnetic fields the intervortex interaction is controlled only by the anisotropy of the London penetration depth, one can always obtain the hexagonal vortex lattice by the coordinate rescaling with the anisotropy factor[72]. To determine the field range where such procedure can give us a reasonable approximation, we perform a rescaling of the vortex lattice images at various fields by fitting the scaling parameter so that to obtain the hexagonal lattice: $x \to x/\sqrt{\kappa}$ and $y \to y\sqrt{\kappa}$, where the parameter κ has meaning of the effective lattice anisotropy. At low fields κ should coincide with the in-plane anisotropy of the London penetration depth. The field dependence of the evaluated scaling ratio κ is shown in the Fig. 5. At low fields, κ is close to one suggesting that the London penetration depth is almost isotropic in the ab plane. Strictly speaking, this procedure is not unique and rescaling with the factor $\kappa \approx 3$ also gives a hexagonal lattice. Neither of these values is consistent with the anisotropy of the vortex core. We find that the effective lattice anisotropy monotonically increases with the magnetic field. Above the field equal to 4 T the scaling ratio becomes independent of the field. It should be noted that both the anisotropy of the vortex core shape (Fig. 2(b)) and the anisotropy of the vortex lattice (Fig. 5(b)) gradually grow in the range 1T$\leq H \leq$ 4T and saturate approximately at $H = 4$T. The ratio κ appears less then the core anisotropy by a factor ~ 1.5 in a wide field range. This can be interpreted assuming, e.g., that the anisotropy of the London penetration depth at high field is affected only by the anisotropy of the hole pocket while the superconductivity in the electron pocket is suppressed.

Our measurements of the density of states inside the vortex core clearly demonstrate a substantial anisotropy of the system: the ratio of the core dimensions is of the order of 2. As a result, to explain the observation of the square vortex lattice at high magnetic field we assume that it arises from the distortion of the hexagonal vortex lattice in the anisotropic superconductor with the anisotropy of the effective masses of the order of $\sqrt{3}$. Strictly speaking the latter anisotropy factor does not coincide with the factor describing the core anisotropy. This discrepancy may be connected with the additional core distortion caused by the gap anisotropy at the Fermi surface which does not necessarily coincide with the anisotropy of the effective masses of the Cooper pairs.

For the qualitative theoretical description of the observed experimental data, we suggest to use a two-band Ginzburg–Landau (GL) model with the interband Josephson coupling. We write the free energy in the following form:

$$F = \int \left\{ \sum_{j=1}^{2} \left[a^{(j)} |\psi^{(j)}|^2 + \frac{b^{(j)}}{2} |\psi^{(j)}|^4 + \left(\mathbf{D}\psi^{(j)}\right)^* \hat{K}^{(j)} \left(\mathbf{D}\psi^{(j)}\right) \right] + \varepsilon_J \left({\psi^{(1)}}^* \psi^{(2)} + {\psi^{(2)}}^* \psi^{(1)} \right) + \frac{\mathbf{B}^2}{8\pi} \right\} dV \quad (1)$$

where $a^{(1,2)}$, $b^{(1,2)}$, $\hat{K}^{(1,2)}$ and ε_J are the phenomenological parameters, $\mathbf{D} = -i\nabla - (2\pi/\Phi_0)\mathbf{A}$. The tensors $\hat{K}^{(1)}$ and $\hat{K}^{(2)}$ in general have different anisotropies, which gives possibility of the transformation of the vortex lattice. This two-band GL model suffers from too many free parameters. Minimization of the free energy and analysis of the phase diagram versus all the parameters of the model seems redundant because it is difficult to verify a particular choice of these parameters. Therefore we consider two simplified cases of parameters which allow to illustrate a possible qualitative explanation of our experimental data by the simplest numerical analysis.

At first we consider the case of vanishing Josephson interband coupling $\varepsilon_J = 0$, so that the order parameter components interact only via the magnetic field in agreement with the conclusions of Refs.[73,74] for FeSe. At the same time we should note that this assumption of zero Josephson coupling contradicts to some recent numerical works (see, e.g.,[68]) modeling FeSe.

Introducing the Cooper pair wavefunctions in different energy bands one can define two critical magnetic fields $H_{c2}^{(1,2)} \sim \Phi_0/(\xi^{(1,2)})^2$ corresponding to the suppression of different order parameter components by the approaching vortex centers. Assuming $H_{c2}^{(2)} < H_{c2}^{(1)}$, we see that a complete suppression of superconductivity in both bands should occur only at the upper critical field $H_{c2}^{(1)}$, while the field $H_{c2}^{(2)}$ corresponds just to a strong suppression of the superconducting correlations in one of the bands. This line of reasoning allows us to assume that it is the interplay between the dominant order parameter $\psi^{(1)}$ and the growing below $H_{c2}^{(2)}$ subdominant order parameter $\psi^{(2)}$ which is responsible both for the kink in the specific heat data and the smooth transformation of vortex lattice structure found in STM measurements.

To illustrate these simple arguments, we consider here a range of fields where one of the order parameter component is dominating while the other is significantly suppressed. Therefore we can use London model for the first component and use the Ginzburg-Landau approach[15] for the second component. Assuming for simplicity the vortex centers in both order parameter components to coincide we can write the free energy of the superconductor as a sum of two terms:

$$F = \frac{1}{8\pi}\int\left[\left(\lambda^{(1)}\right)^2 \operatorname{curl}\mathbf{B}\hat{m}^{(1)}\operatorname{curl}\mathbf{B}+\mathbf{B}^2\right]dV+ \frac{\left(H_{cm}^{(2)}\right)^2}{4\pi}\int dV\left[-\left|\psi^{(2)}\right|^2+\frac{1}{2}\left|\psi^{(2)}\right|^4+ \left(\xi^{(2)}\right)^2\left(\mathbf{D}\psi^{(2)}\right)^*\left(\hat{m}^{(2)}\right)^{-1}\left(\mathbf{D}\psi^{(2)}\right)\right]. \quad (2)$$

Here we introduce the normalized mass tensors $\hat{m}^{(1)}$ and $\hat{m}^{(2)}$ following[72]. We consider a strong type-II superconductor with $\lambda^{(1,2)} \gg \xi^{(1,2)}$. Both tensors $\hat{m}^{(1)}$ and $\hat{m}^{(2)}$ are determined by the crystal symmetry meaning that they both can be diagonalized in the same axes. The lattice structure should depend on the field if these tensors have different anisotropy. At the high fields above $H_{c2}^{(2)} = \Phi_0/(2\pi(\xi^{(2)})^2)$ the lattice is completely described by the anisotropy of $\hat{m}^{(1)}$. Below this field the second component comes into play starting to modify the structure of the vortex lattice. In the case $\xi^{(1)} \ll \xi^{(2)} \ll \lambda^{(2)} \ll \lambda^{(1)}$ the total effective penetration length is determined mostly by the $\lambda^{(2)}$ value in the low fields. Thus, the structure of the vortex lattice should be consistent with the anisotropy of the tensor $m^{(2)}$. In order to describe the transition from the hexagonal lattice at low fields to the distorted square lattice at high fields we take for illustration the isotropic $\hat{m}^{(2)}$ and $m_x^{(1)}/m_y^{(1)} \sim 3$.

The field dependence of the angles of the unit cell of the vortex lattice calculated using this model are shown on the Fig. 6. Above the field $H_{c2}^{(2)}$ the lattice does not experience any modifications. The transformation occurs close to the field $H^* \sim 0.7H_{c2}^{(2)}$ which is below the critical field $H_{c2}^{(2)}$.

In the above model we did not consider possible splitting in positions of vortices in two components of the order parameter. However, this splitting has not been observed in the LDOS patterns which clearly do not show the doubling of the vortex images.

Now we proceed with the consideration of the opposite limit of strong Josephson coupling $|\varepsilon_J| \gg |a^{(1,2)}|$. Applying the linear transformation for the order parameters components $\psi^{(1)} = \eta^{(1)}\cos\alpha - \eta^{(2)}\sin\alpha$, $\psi^{(2)} = \eta^{(1)}\sin\alpha + \eta^{(2)}\cos\alpha$ one can exclude the Josephson term from the free energy expression written through the new components ${\eta^{(1)}}^*\eta^{(2)} + c.c.$. In terms of the new order parameter components $\eta^{(1,2)}$ the free energy takes the following form:

$$F = \int\left\{\sum_{j=1}^{2}\left[\tilde{a}^{(j)}|\eta^{(j)}|^2+ \left(\mathbf{D}\eta^{(j)}\right)^*\hat{\tilde{K}}^{(j)}\left(\mathbf{D}\eta^{(j)}\right)\right]+ \left(\mathbf{D}\eta^{(1)}\right)^*\hat{\tilde{K}}^{(12)}\left(\mathbf{D}\eta^{(2)}\right)+c.c. \right. \left. f_4\left(\eta^{(1)},\eta^{(2)}\right)+\frac{\mathbf{B}^2}{8\pi}\right\}dV\ , \quad (3)$$

where f_4 contains all the fourth-order terms of $\eta^{(1)}$ and $\eta^{(2)}$. In the case of the strong Josephson interaction the parameters $\tilde{a}^{(1)}$ and $\tilde{a}^{(2)}$ have different signs (for certainty $\tilde{a}^{(1)} < 0$ and $\tilde{a}^{(2)} > 0$), i.e. the $\eta^{(2)}$ component is significantly suppressed. Further analysis can be simplified close to the upper critical field H_{c2}, where the linear equations for the order parameter components have the following form:

$$\tilde{a}^{(2)}\eta^{(2)} + \mathbf{D}\hat{\tilde{K}}^{(12)}\mathbf{D}\eta^{(1)} = 0 \quad (4)$$

$$\tilde{a}^{(1)}\eta^{(1)} + \mathbf{D}\hat{\tilde{K}}^{(1)}\mathbf{D}\eta^{(1)} - \frac{1}{\tilde{a}^{(2)}}\left(\mathbf{D}\hat{\tilde{K}}^{(12)}\mathbf{D}\right)^2\eta^{(1)} = 0\ . \quad (5)$$

Here we have neglected the term proportional to $\hat{\tilde{K}}^{(2)}$ assuming non-gradient term to be more significant. Thus, in the limit of the magnetic field close to the upper critical field the two component GL model can be effectively reduced to the single component model with the non-local gradient terms. The anisotropy of the tensors $\hat{\tilde{K}}^{(1)}$ and $\hat{\tilde{K}}^{(12)}$ is different in the general case so these non-local terms can lead to the vortex lattice transformation. The analysis of the GL model with the non-local term is given in the Appendix A.

Finally, another possible reason for the observed vortex lattice transformation is related to the "magneto-elastic" interactions, which appear because when the normal cores are nucleated they push slightly on the surrounding superconducting phase. Therefore, there is an additional contribution to intervortex interactions due to the strain field generated by vortices. This interaction is weak but long-ranged and affects the vortex lattice in materials with large dT_c/dp, where p is pressure or strain [75]. In fact, one might need to include this interaction even to understand the vortex lattice in tilted fields in $NbSe_2$ with $dT_c/dp \sim 0.5$ K/GPa, because the standard anisotropic London in this case gives the wrong answer for VLs[76]. For iron-based materials, dT_c/dp is on the order of K/GPa and varies with doping[77]. Hence, all these materials are good candidates for observing the vortex structure evolution and transitions caused by strain induced interactions. A square vortex lattice transition has recently been reported in LiFeAs[78] and it has been explained in terms of vortex overlap. The different shape of the vortex cores and strong differences in the band structure in these two compounds make it rather difficult to

give the comparison of FeSe and LiFeAs. Further experimental work is necessary to compare the scenario of the vortex lattice transformations in these systems and clarify the relevance of the multigap order parameter structure for the case of LiFeAs. We have carefully analyzed our data and we can safely exclude this as a possible origin of the vortex lattice transformation in FeSe. We do not observe any vortex overlap in our STM data at fields below 3T, which is a field higher than the field region in which the vortex lattice smoothly changes from nearly hexagonal to rhombic. However the issue of vortex core overlapping deserves a more detailed comment if we keep in mind that in our model there are two components of the order parameter. The dominant component is highly anisotropic and provides the square-like lattice at the high field. Its coherence length is definitely smaller than the distance between vortices because we work far from the upper critical field H_{c2} of the superconductor. The subdominant component of the order parameter is assumed to be isotropic and the upper critical field $H_{c2}^{(2)}$ for this component is less than H_{c2}. The size of the vortex core is different for different order parameter components. Thus, for our range of magnetic fields below the field $H_{c2}^{(2)}$ the cores overlap if we consider the subdominant order parameter pattern and do not overlap for the dominant order parameter component. It is the overlapping of the subdominant order parameter cores which is responsible for the transformation of the vortex lattice to the hexagonal one at low magnetic field. The STM measurements appear to be sensitive mainly to the dominant order parameter component which we associate with Γ pocket and thus our experiments do not show the overlap of the vortex cores in the field range where the rhombic distortion of the vortex lattice are observed.

IV. IV. CONCLUSIONS

In summary we have studied vortex core and vortex lattice in FeSe single crystals. We observed an elliptical vortex core with an anisotropy that increases in applied magnetic field. Tunneling spectra in the vortex core reveal the presence of low-energy excitation states that are particle-hole asymmetric along the long direction of the vortex core and the local density of states shows spatial oscillatory behavior. Such features are characteristic of vortex core in the quantum limit. Furthermore, the evolution of the vortex lattice as a function of magnetic field shows strong deformations from an almost hexagonal to nearly square lattice above the field ~ 1.5 T applied perpendicular to the a-b plane of the sample. Several features of the vortex core and vortex lattice appear unexpected and they can be explained only if one considers a compensation effect due to the multiband nature of this material. First, the anisotropy of the vortex core is quantitatively different from the gap anisotropy and the anisotropy of the Γ pocket. One needs to consider possible contributions from the electron pocket to explain the observed anisotropy. Second, the nearly hexagonal vortex lattice at low field is unexpected in a material with orthorhombic crystal structure and it is in contradiction with the elliptical vortex core. Therefore, the anisotropy of the penetration depth and that of the coherence length appear to be different at low field. However, at high field this anisotropy is the same ((Fig. 5(b))). Finally, the observed rhombic distortions of the vortex lattice appear to happen in a field region where a kink is observed in the magnetic field dependence of the specific heat ((Fig. 4(a) and (b))). This kink of the specific heat suggests that one of the order parameter components is suppressed at high fields. This assumption along with choice of different anisotropies of the effective masses in different bands allow to reproduce qualitatively the transformation of the vortex lattice. While we cannot exclude contributions from other sources to the vortex lattice transformation, it seems that the multiband nature is playing an important role to reconcile some of the apparent contradictions. Other possible contributions to the vortex lattice transformation are nonlocal effects and magneto-elastic interaction.

V. ACKNOWLEDGEMENTS

The authors would like to acknowledge fruitful discussions with V. Kogan and T. Hanaguri. We also would like to acknowledge technical support during the early stage of these measurements from S. A. Moore. The work at Temple University, where low temperature scanning tunneling measurements were performed, was supported by U.S. Department of Energy, Office of Science, Basic Energy Science, Materials Sciences and Engineering Division under Award Number DE-SC0004556. The work at Drexel University and at the M.V. Lomonosov Moscow State University was supported by the U.S, Civilian Research and Development Foundation (CRDF Global). The work in Russia has been supported in part by the Ministry of Education and Science of the Russian Federation in the framework of the Increase Competitiveness Program of NUST MISiS grant K2-2017-084, by Act 211 of the Government of Russian Federation, Contracts No. 02.A03.21.0004, 02.A03.21.0006, 02.A03.21.0011 and by the Russian Government Program of Competitive Growth of Kazan Federal University. One of the authors (C.D.G.) would like to acknowledge partial support from MIUR (Ministry of Education, Universities and Research of the Italian Government). The work in IPM RAS (Nizhny Novgorod) was supported in part by the Russian Science Foundation (the calculation of the vortex lattice characteristics Grant No. 187210027; the calculation of the vortex core deformation and the analysis of the experimental data Grant No. 171201383), the Russian Foundation for Basic Research (Grant No. 175212044), and Foundation for the advancement of theoretical physics BASIS No. 109. The work at Argonne National Laboratory was supported by the U.S. Depart-

ment of Energy, Office of Science, Basic Energy Science, Materials Sciences and Engineering Division.

* Present address: Institute for Physics of Microstructures RAS, Nizhny Novgorod, GSP-105, Russia 603950
† Present address: E.R. Caianiello Physics Department and NANOMATES, Research Centre for Nanomaterials and Nanotechnology, University of Salerno, Fisciano (SA), Italy

[1] N. B. Kopnin. *Theory of nonequilibrium superconductivity.* (Oxford University Press, (2001).
[2] N. E. Hussey, *Low-energy quasiparticles in high-T_c cuprates.* Adv. Phys. **51**, 1685-1771 (2002).
[3] H. F. Hess, R. B. Robinson, R. C. Dynes, J. M. Valles, and J. V. Waszczak, *Scanning-Tunneling-Microscope Observation of the Abrikosov Flux Lattice and the Density of States near and inside a Fluxoid.* Phys. Rev. Lett. **62**, 214-216 (1989).
[4] H. Hess, R. Robinson, and J. Waszczak, *Vortex-core structure observed with a scanning tunneling microscope.* Phys. Rev. Lett. **64**, 2711-2714 (1990).
[5] H. Nishimori, K. Uchiyama, S. Kaneko, A. Tokura, H. Takeya, K. Hirata, and N. Nishida, *First observation of the fourfold-symmetric and quantum regime vortex core in YNi_2B_2C by scanning tunneling microscopy and spectroscopy* J. Phys. Soc. Japan **73**, 3247 (2004).
[6] S. Kaneko, K. Matsuba, M. Hafiz, K. Yamasaki, E. Kakizaki, N. Nishida, H. Takeya, K. Hirata, T. Kawakami, T. Mizushima, K. Machida, *Quantum Limiting Behaviors of a Vortex Core in an Anisotropic Gap Superconductor.* J. Phys. Soc. Japan **81**, 063701 (2012).
[7] J. E. Hoffman, E. W. Hudson, K. M. Lang, V. Madhavan, H. Eisaki, S. Uchida, and J. C. Davis, *A four unit cell periodic pattern of quasi-particle states surrounding vortex cores in $Bi_2Sr_2CaCu_2O_{8+\delta}$.* Science **295**, 466 (2002).
[8] B. B. Zhou, S. Misra, E. H. da Silva Neto, P. Aynajian, R. E. Baumbach, J. D. Thompson, E. D. Bauer, and A. Yazdani, *Visualizing nodal heavy fermion superconductivity in $CeCoIn_5$.* Nature Phys. **9**, 474 (2013).
[9] M. P. Allan, F. Massee, D. K. Morr, J. Van Dyke, A. W. Rost, A. P. Mackenzie, C. Petrovic, and J. C. Davis, *Imaging Cooper pairing of heavy fermions in $CeCoIn_5$.* Nature Phys. **9**, 468 (2013).
[10] K. Izawa, H. Yamaguchi, Y. Matsuda, H. Shishido, R. Settai, and Y. Onuki, *Angular position of nodes in the superconducting gap of quasi-2D heavy-fermion superconductor $CeCoIn_5$.* Phys. Rev. Lett. **87**, 057002 (2001).
[11] C.-L. Song, Y.-L. Wang, P. Cheng, Y.-P. Jiang, W. Li, T. Zhang, Z. Li, K. He, L. Wang, J.-F. Jia, H.-H. Hung, C. Wu, X. Ma, X. Chen, and Q.-K. Xue, *Direct observation of nodes and twofold symmetry in FeSe superconductor.*, Science **332**, 1410-1413 (2011).
[12] T. Watashige, Y. Tsutsumi, T. Hanaguri, Y. Kohsaka, S. Kasahara, A. Furusaki, M. Sigrist, C. Meingast, T. Wolf, H. v. Lohneysen, T. Shibauchi, and Y. Matsuda, *Evidence for Time-Reversal Symmetry Breaking of the Superconducting State near Twin-Boundary Interfaces in FeSe Revealed by Scanning Tunneling Spectroscopy.* Phys. Rev. X **5**, 031022 (2015).
[13] H.H. Hung, C.-L. Song, X. Chen, X. Ma, Q.K. Xue, and C. Wu, *Anisotropic vortex lattice structures in the FeSe superconductor* Phys. Rev. B **85**, 104510 (2012).
[14] D. Chowdhury, E. Berg, and S. Sachdev, *Nematic order in the vicinity of a vortex in superconducting FeSe* Phys. Rev. B **84**, 205113 (2011).
[15] A. A. Abrikosov, *On the Magnetic Properties of Superconductors of the Second Group.* Zh. Eksp. Teor. Fiz. **32**, 1442 (1957) [Sov. Phys. JETP **5**, 1174 (1957)].
[16] W.H. Kleiner, L.M. Roth, and S.H. Autler, *Bulk Solution of Ginzburg-Landau Equations for Type* 2 *Superconductors-Upper Critical Field Region.* Phys. Rev.A-General Physics **133**, A1226 (1964).
[17] Y. De Wilde, M. Iavarone, U. Welp, V. Metlushko, A.E. Koshelev, I. Aranson, G.W. Crabtree, P. Canfield, *Scanning tunneling microscopy observation of a square Abrikosov lattice in $LuNi_2B_2$* Phys. Rev. Lett. **78**, 4273 (1997).
[18] M. R. Eskildsen, C. D. Dewhurst, B. W. Hoogenboom, C. Petrovic, and P. C. Canfield, *Hexagonal and square flux line lattices in $CeCoIn_5$* Phys. Rev. Lett. **90**, 187001 (2003).
[19] A.J.Berlinsky, A.L. Fetter, M. Franz, C. Kallin, and P.I. Soininen, *Ginzburg-Landau Theory of Vortices in d-wave Superconductors* Phys. Rev. Lett. **75**, 2200 (1995).
[20] J. Shiraishi, M. Kohmoto, and K. Maki, *Vortex lattice transition in d-wave superconductors.* Phys. Rev. B **59**, 4497 (1999).
[21] M. Ichioka, A. Hasegawa, and K. Machida, *Field dependence of the vortex structure in d-wave and s-wave superconductors.* Phys. Rev. B **59**, 8902 (1999).
[22] V. G. Kogan, A. Gurevich, J. H. Cho, D. C. Johnston, M. Xu, J. R. Thompson, and A. Martynopvich, *Nonlocal electrodynamics and low-temperature magnetization of clean high-kappa superconductors.* Phys. Rev. B **54**, 12386 (1996).
[23] V. G. Kogan, M. Bullock, B. Harmon, P. Miranovic, Lj. Dobrosavljevic-Grujic, P. L. Gammel, and D. J. Bishop, *Vortex lattice transitions in borocarbides* Phys. Rev. B **55**, R8693 (1997).
[24] V. G. Kogan, P. Miranovic, Lj. Dobrosavljevic-Grujic, W.E. Pickett, and D. K. Christen, *Vortex lattices in cubic superconductors.* Phys. Rev. Lett. **79**, 741 (1997).
[25] X. Yang, Z. Du, H. Lin, D. Fang, H. Yang, X. Zhu, and H-H Wen *Vortex lattice and vortex bound states in $CsFe_2As_2$ investigated by scanning tunneling microscopy/spectroscopy.* Phys. Rev. B **98**, 024505 (2018).
[26] G. Karapetrov, J. Fedor, M. Iavarone, D. Rosenman, and W. Kwok, *Direct observation of geometrical phase transitions in mesoscopic superconductors by scanning tunneling microscopy.* Phys. Rev. Lett. **95**, 167002 (2005).
[27] M. Iavarone, R. Di Capua, G. Karapetrov, D. Rosenmann, H. Claus, C. D. Malliakas, M. G. Kanatzidis, T. Nishizaki, and N. Kobayashi, *Effect of magnetic impurities on the vortex lattice properties in $NbSe_2$ single crystals* Phys. Rev. B **78**, 174518 (2008).
[28] C.-L. Song, Y.-L. Wang, Y.-P. Jiang, L. Wang, K. He, X. Chen, J.E. Hoffman, X.-C. Ma, and Q.-K. Xue, *Suppression of Superconductivity by Twin Boundaries in FeSe.* Phys. Rev. Lett. **109**, 137004 (2012).

[29] A. E. Böhmer and A. Kreisel, *Nematicity, magnetism and superconductivity in FeSe* Journal of Physics: Condensed Matter **30**, 023001 (2018).

[30] J. Maletz, V. B. Zabolotnyy, D. V. Evtushinsky, S. Thirupathaiah, A. U. B. Wolter, L. Harnagea, A. N. Yaresko, A. N. Vasiliev, D. A. Chareev, A. E. Böhmer, F. Hardy, T. Wolf, C. Meingast, E. D. L. Rienks, B. Büchner, and S. V. Borisenko, *Unusual band renormalization in the simplest iron-based superconductor* $FeSe_{1-x}$. Phys. Rev. B **89**, 220506(R) (2014).

[31] M. D. Watson, T. K. Kim, A. A. Haghighirad, N. R. Davies, A. McCollam, A. Narayanan, S. F. Blake, Y. L. Chen, S. Ghannadzadeh, A. J. Schofield, M. Hoesch, C. Meingast, T. Wolf, and A. I. Coldea, *Emergence of the nematic electronic state in FeSe.* Phys. Rev. B **91**, 155106 (2015).

[32] M. D. Watson, T. K. Kim, A. A. Haghighirad, S. F. Blake, N. R. Davies, M. Hoesch, T. Wolf, and A. I. Coldea, *Suppression of orbital ordering by chemical pressure in* $FeSe_{1-x}S_x$ *Phys. Rev. B* **92**, 121108 (2015).

[33] T. Terashima, N. Kikugawa, A. Kiswandhi, E.-S. Choi, J. S. Brooks, S. Kasahara, T. Watashige, H. Ikeda, T. Shibauchi, Y. Matsuda, T. Wolf, A. E. Böhmer, F. Hardy, C. Meingast, H. v. Löhneysen, M.-T. Suzuki, R. Arita, and S. Uji, *Anomalous Fermi surface in FeSe seen by Shubnikov-de Haas oscillation measurements* Phys. Rev. B **90**, 144517 (2014).

[34] Y. S. Kushnirenko, A. V. Fedorov, E. Haubold, S. Thirupathaiah, T. Wolf, S. Aswartham, I. Morozov, T. K. Kim, B. Büchner, and S. V. Borisenko *Three-dimensional superconducting gap in FeSe from angle-resolved photoemission spectroscopy* Phys. Rev. B **97**, 180501(R) (2018).

[35] A.I. Coldea and M. D. Watson, *The Key Ingredients of the Electronic Structure of FeSe* Annu. Rev. Condens. Matter Phys. **9**, 125-146 (2018).

[36] D. Chareev, E. Osadchii, T. Kuzmicheva, J. Y. Lin, S. Kuzmichev, O. Volkova, and A. Vasiliev, *Single crystal growth and characterization of tetragonal* $FeSe_{1-x}$ *superconductors.* Cryst. Eng. Comm **15**, 1989 (2013).

[37] D. Huang, T.A. Webb, C.-L. Song, C.-Z. Chang, J.S. Moodera, E. Kaxiras and J.E. Hoffman, *Dumbbell Defects in FeSe Films: A Scanning Tunneling Microscopy and First-Principles Investigation.* Nano Lett. **16**, 4224 (2016).

[38] 1. T.M. McQueen, A.J. Williams, P.W. Stephens, J. Tao, Y. Zhu, V. Ksenofontov, F. Casper, C. Felser and R.J. Cava, *Tetragonal-to-Orthorhombic Structural Phase Transition at* 90 *K in the Superconductor* $Fe_{1.01}Se$ Phys. Rev. Lett. **103**, 057002 (2009).

[39] N. Hayashi, M. Ichioka, and K. Machida, *Star-Shaped Local Density of States around Vortices in a Type-II Superconductor* Phys. Rev. Lett. **77**, 4074 (1996).

[40] N. Hayashi, M. Ichioka, and K. Machida, *Effects of gap anisotropy upon the electronic structure around a superconducting vortex* Phys. Rev. B **56**, 9052 (1997).

[41] F. Gygi and M. Schluter, *Angular band structure of a vortex line in a type-II superconductor Phys. Rev. Lett.* **65**, 1820 (1990).

[42] F. Gygi and M. Schluter, *Self-consistent electronic structure of a vortex line in a type-II superconductor Phys. Rev. B* **43**, 7609 (1991).

[43] Y. D. Zhu, F. C. Zhang, and M. Sigrist, *Electronic structure of a vortex line in a type-II superconductor: Effect of atomic crystal fields* Phys. Rev. B **51**, 1105 (1995).

[44] N. Nakai, P. Miranović, M. Ichioka, and K. Machida, *Reentrant Vortex Lattice Transformation in Fourfold Symmetric Superconductors* Phys. Rev. Lett. **89**, 237004 (2002).

[45] Y. Wang, P. J. Hirschfeld, and I. Vekhter, *Theory of quasiparticle vortex bound states in iron-based superconductors: Application to scanning tunneling spectroscopy of LiFeAs* Phys. Rev. B **85**, 020506 (2012).

[46] C. Caroli, P. G. De Gennes and J. Matricon, *Bound Fermion states on a vortex line in a type II superconductor.* Phys. Lett. **9**, 307 (1964).

[47] S. H. Pan, et al. *STM Studies of the Electronic Structure of Vortex Cores in* $Bi_2Sr_2CaCu_2O_{8+\delta}$ Phys. Rev. Lett. **85**, 1536-1539 (2000).

[48] I. Maggio-Aprile, Ch. Renner, A. Erb, E. Walker, Ø Fischer, *Direct Vortex Lattice Imaging and Tunneling Spectroscopy of Flux Lines on* $YBa_2Cu_3O_7$ Phys. Rev. Lett. **75**, 2754-2757 (1995).

[49] Lei Shan, Yong-Lei Wang, Bing Shen, Bin Zeng, Yan Huang, Ang Li, Da Wang, Huan Yang, Cong Ren, Qiang-Hua Wang, Shuheng H. Pan and Hai-Hu Wen *Observation of ordered vortices with Andreev bound states in* $Ba_{0.6}K_{0.4}Fe_2As_2$ Nat. Phys. **7**, 325-331 (2011).

[50] T. Hanaguri, K. Kitagawa, K. Matsubayashi, Y. Mazaki, Y. Uwatoko, and H. Takagi *Scanning tunneling microscopy/spectroscopy of vortices in LiFeAs* Phys. Rev. B **85**, 214505 (2012).

[51] F. Massee,Peter O. Sprau, Y.-L. Wang, J. C. S. Davis, G. Ghigo, G. Gu, Wai-Kwong Kwok *Imaging atomic-scale effects of high-energy ion irradiation on superconductivity and vortex pinning in Fe(Se,Te)* Sci. Adv. **1**, e1500033 (2015).

[52] M. Chen, X. Chen, H. Yang, Z. Du, X. Zhu, E. Wang and H.-H. Wen, *Discrete energy levels of Caroli-de Gennes-Matricon states in quantum limit in* $FeTe_{0.55}Se_{0.45}$ Nature Communications **9**, 970 (2018).

[53] N. Hayashi, T. Isoshima, M. Ichioka, and K. Machida, *Low-Lying Quasiparticle Excitations around a Vortex Core in Quantum Limit* Phys. Rev. Lett. **80**, 2921 (1998).

[54] S. Kasahara, T. Watashige, T. Hanaguri, Y. Kohsaka, T. Yamashita, Y. Shimoyama, Y. Mizukami, R. Endo, H. Ikeda, K. Aoyama, T. Terashima, S. Uji, T. Wolf, H. von Löhneysen, T. Shibauchi and Y. Matsuda, *Field-induced superconducting phase of FeSe in the BCS-BEC cross-over* Proc. Natl Acad. Sci. **111**, 16309 (2014).

[55] V. G. Kogan, and N. V. Zhelezina, *Field dependence of the vortex core size* Phys. Rev. B **71**, 134505 (2005).

[56] J.E. Sonier, *Investigations of the core structure of magnetic vortices in type-II superconductors using muon spin rotation* J. Phys. Condens. Matter **16**, S4499 (2004).

[57] P. O. Sprau, A. Kostin, A. Kreisel, A. E. Böhmer, V. Taufour, P. C. Canfield, S. Mukherjee, P. J. Hirschfeld, B. M. Andersen, J.C. S. Davis, *Discovery of orbital-selective Cooper pairing in FeSe* Science **357**, 75 (2017).

[58] A. Fente, E. Herrera, I. Guillamon, H. Suderow, S. Manas-Valero, M. Galbiati, E. Coronado, and V. G. Kogan, *Field dependence of the vortex core size probed by scanning tunneling microscopy* Phys. Rev. B **94**, 014517 (2016).

[59] U. Hartmann, A. A. Golubov, T. Drechsler, M. Yu. Kupriyanov, and C. Heiden, *Measurement of the Vortex-Core Radius By Scanning-Tunneling-Microscopy* Phys. B **194**, 387 (1994).

[60] A. Fente, W. R. Meier, T. Kong, V. G. Kogan, S. L. Bud'ko, P. C. Canfield, I. Guillamon, H. Suderow, *Influence of multiband sign-changing superconductivity on*

vortex cores and vortex pinning in stoichiometric high-Tc $CaKFe_4As_4$ Phys. Rev. B **97**, 134501 (2018).

[61] R. Joynt and L. Taillefer, *The superconducting phases of UPt_3* Rev. Mod. Phys **74**, 235 (2002).

[62] G. E. Volovik, *Superconductivity with Lines of Gap Nodes - Density-of-States in the Vortex* JETP Lett. **58**, 469 (1993).

[63] Y. Sun, S. Kittaka, S. Nakamura, T. Sakakibara, K. Irie, T. Nomoto, K. Machida, J. Chen, and T. Tamegai, *Gap structure of FeSe determined by angle-resolved specific heat measurements in applied rotating magnetic field* Phys. Rev. B **96**, 220505(R) (2017).

[64] S. A. Moore, J. L. Curtis, C. Di Giorgio, E. Lechner, M. Abdel-Hafiez, O. S. Volkova, A. N. Vasiliev, D. A. Chareev, G. Karapetrov, and M. Iavarone, *Evolution of the superconducting properties in $FeSe_{1x}S_x$* Phys. Rev. B **92**, 235113 (2015).

[65] M. Abdel-Hafiez, Y.-Y. Zhang, Z.-Y. Cao, C.-G. Duan, G. Karapetrov, V. M. Pudalov, V. A. Vlasenko, A. V. Sadakov, D. A. Knyazev, T. A. Romanova, D. A. Chareev, O. S. Volkova, A. N. Vasiliev, and Xiao-Jia Chen, *Superconducting properties of sulfur-doped iron selenide* Phys. Rev. B **91**, 165109 (2015).

[66] F. Bouquet, Y. Wang, I. Sheikin, T. Plackowski, A. Junod, S. Lee, and S. Tajima, *Specific Heat of Single Crystal MgB_2: A Two-Band Superconductor with Two Different Anisotropies* Phys. Rev. Lett. **89** 257001 (2002).

[67] Y. Nakajima, H. Hidaka, T. Nakagawa, T. Tamegai, T. Nishizaki, T. Sasaki, and N. Kobayashi, *Two-band superconductivity featuring different anisotropies in the ternary iron silicide $Lu_2Fe_3Si_5$* Phys. Rev. B **85**, 174524 (2012).

[68] A. Kreisel, B. M. Andersen, P. O. Sprau, A. Kostin, J. C. Davis, and P. J. Herschfeld, *Orbital selective pairing and gap structures of iron-based superconductors* Phys. Rev. B **95**, 174504 (2017).

[69] V. Moshchalkov, M. Menghini, T. Nishio, Q. H. Chen, A. V. Silhanek, V. H. Dao, L. F. Chibotaru, N. D. Zhigadlo, and J. Karpinski, *Type*-1.5 *Superconductivity* Phys. Rev. Lett. **102**, 117001 (2009).

[70] E. Babaev, J. Carlstrom, and J. M. Speight, *Type*-1.5 *Superconducting State from an Intrinsic Proximity Effect in Two-Band Superconductors* Phys. Rev. Lett. **105**, 067003 (2010).

[71] A. S. Mel'nikov, *Phase-Transitions in the Flux Line Lattices of Hexagonal Unconventional Superconductors* JETP **74**, 1059 (1992); ZhETF **101**, 1978 (1992).

[72] *Vortex lattice structures in uniaxial superconductors* L. J. Campbell, M. M. Doria, and V. G. Kogan, Phys. Rev. B **38**, 2439 (1988).

[73] *Evolution of Two-Gap Behavior of the Superconductor $FeSe_{1x}$* R. Khasanov, M. Bendele, A. Amato, K. Conder, H. Keller, H.-H. Klauss, H. Luetkens, and E. Pomjakushina, Phys. Rev. Lett. **104**, 087004 (2010).

[74] *Two-Band Superconductors: Hidden Criticality Deep in the Superconducting State* L. Komendová, Yajiang Chen, A. A. Shanenko, M. V. Milošević, and F.M. Peeters, Phys. Rev. Lett. **108**, 207002 (2012).

[75] Shi-Zeng Lin and V. G. Kogan, *Strain-induced intervortex interaction and vortex lattices in tetragonal superconductors* Phys. Rev. B **95**, 054511 (2017).

[76] V. G. Kogan, L. N. Bulaevskii, P. Miranovic, and L. Dobrosavljevic-Grujić, *Vortex-induced strain and flux lattices in anisotropic superconductors* Phys. Rev. B **51**, 15344 (1995).

[77] E. Gati, S. Kohler, D. Guterding, B. Wolf, S. Knöner, S. Ran, S. L. Bud'ko, P. C. Canfield, and M. Lang, *Hydrostatic-pressure tuning of magnetic, nonmagnetic, and superconducting states in annealed $Ca(Fe_{1x}Co_x)_2As_2$* Phys. Rev. B **86**, 220511 (2012).

[78] J. Yin, S.S. Zhang, G. Dai, H. Zheng, G. Chang, I. Belopolski, X. Wang, H.Lin, Z. Wang, C. Jin, M. Z. Hasan *Vector field based emergent phase diagram in a correlated superconductor* arXiv:1802.10059

[79] K. Takanaka. *Magnetization and Flux Line Lattice in Anisotropic Superconductors*. In: Weber H.W. (eds) *Anisotropy Effects in Superconductors*. (Springer, Boston, MA, 93-112 (1977)).

[80] D. Saint-James, G. Sarma and E. J. Thomas. *Type II Superconductivity*. (Elsevier Science & Technology, (1969)).

VI. APPENDIX A

In order to describe the field-dependent distortion of the vortex lattice above the critical filed H^* we follow the Ref.[79] and introduce the Ginzburg-Landau free energy per the unit vortex length modified taking account of the higher-order gradient terms responsible for the nonlocal response of the superconducting condensate:

$$F = \frac{H_{cm}^2}{4\pi}\int\Big\{-|\psi|^2+\frac{1}{2}|\psi|^4+\xi^2|\mathbf{D}\psi|^2+ \xi^4|\mu_{xx}D_x^2\psi+\mu_{yy}D_y^2\psi|^2+ \xi^4\mu_{xy}^2\left[(D_x^2\psi)^*(D_y^2\psi)+(D_xD_y\psi)^*(D_xD_y\psi)+ +(D_xD_y\psi)^*(D_yD_x\psi)+c.c.\right]\Big\}\,dx\,dy\ , \quad (6)$$

where $\mathbf{D}=-i\nabla-\frac{2\pi}{\Phi_0}\mathbf{A}$, $\mathbf{A}$ is the vector potential of the magnetic field, H_{cm} is the thermodynamic critical field. Due to the large value of the Ginzburg-Landau parameter $\varkappa=\lambda/\xi$ we can neglect the contribution to the magnetic field arising from the supercurrents in the sample and assume the magnetic field to be homogeneous. The usual effective mass term determines the properties of the vortex lattice at low fields while the fourth-order terms originating from the non-local effects affect the properties of the vortex lattice and the vortex core shape at higher fields. Our experimental data provide evidence for the almost hexagonal vortex lattice at low fields and, thus, we assume the effective mass term to be isotropic. The D_{2h} symmetry of the vortex lattice allows to reduce the number of the components in the tensor of fourth-order gradient terms only to three coefficients. The terms with μ_{xx} and μ_{yy} have the D_{2h} symmetry while the last term proportional to μ_{xy}^2 has the D_{4h} symmetry. All these terms are responsible for the distortions of the vortex cores and the vortex lattice.

For the sake of simplicity we follow the original approach introduced by Abrikosov[15] in order to obtain the geometry of the vortex lattice at high fields close to the upper critical field. We start from the linear theory and find the form of the superconducting nuclei:

$$\mathbf{D}^2\psi+\xi^2\left[\mu_{xx}D_x^2+\mu_{yy}D_y^2\right]^2\psi+ \xi^2\mu_{xy}^2\left[D_x^2D_y^2+(D_xD_y)^2+ D_yD_x^2D_y+D_xD_y^2D_x+ (D_yD_x)^2+D_y^2D_x^2\right]\psi=\frac{h}{\xi^2}\psi \quad (7)$$

The h is the lowest eigenvalue of the operator in the left hand side of the above equation. The equation $h(H)=1$ gives the value of the upper critical field. If no high gradient terms are taken into account, i.e. $\mu_{xx}=\mu_{xy}=\mu_{yy}=0$ then we get standard expressions $h=2\pi\xi^2H/\Phi_0$ and $H_{c2}=\Phi_0/(2\pi\xi^2)$.

We choose the vector potential as follows $A_{y'}=Hx'$ where

$$x=x'\cos\alpha-y'\sin\alpha \quad (8)$$
$$y=x'\sin\alpha+y'\cos\alpha \quad (9)$$

The angle α stands for the mutual orientation of the vortex lattice and the anisotropy axis of the fourth order gradient terms in the GL free energy. In general the eigenfunction has the form:

$$\Psi_k(x',y')=e^{iky'}\Psi_0\left(x'-\frac{k}{H}\right)\ , \quad (10)$$

where function Ψ_0 obeys the following equation:

$$-\frac{d^2\Psi_0}{dx'^2}+H^2x'^2\Psi_0+L_4\left(\frac{d}{dx'},x',\alpha\right)\Psi_0=\frac{h}{\xi^2}\Psi_0\ , \quad (11)$$

where L_4 is the fourth order polynomial operator of d/dx' and x' which comes from the high gradient terms after rotation by angle α. This equation coincides with the Schrodinger equation for the harmonic oscillator with the polynomial perturbation. This equation is too complicated to solve exactly but one can use the perturbation theory if the coefficients μ_{xx}, μ_{xy} and μ_{yy} are small enough. Then we consider the function $\Psi_0(x')$ to be expanded as $\Psi_0(x')=\Psi_0^{(0)}(x')+\Psi_0^{(1)}(x')+\ldots$ where $\Psi_0^{(0)}(x')$ is the wavefunction of the ground state of the harmonic oscillator and $\Psi_0^{(1)}(x')$ is the first order perturbation with respect to the operator L_4. The correction to h also can be obtained within the perturbation approach.

As a next step we look for the solution in the following form:

$$\psi(x',y')=\sum_n C_n e^{iknx'}\Psi_0\left(x'-\frac{kn}{H}\right)\ . \quad (12)$$

One can see that this function is periodic $\psi(x',y')=\psi(x',y'+2\pi/k)$. The angle α and the number k determine one of the lattice basis vectors with respect to the anisotropy axes. If we put $C_n=\exp(-i\pi\rho n^2)$ we find out that $|\psi(x',y')|=|\psi(x'+k/H,y'+2\pi\rho/k)|$. Taking $\sigma=k^2/(2H)$ we have a standard (ρ,σ) parametrization of the vortex lattice[80]. Finally we have that the lattice is determined by three real parameters α, ρ and k.

We should minimize the GL free energy in order to find the proper parameters. If we substitute the solution to the free energy functional then we find:

$$F=\int\left[(h-1)|\psi|^2+\frac{1}{2}|\psi|^4\right]\,dx\,dy\ . \quad (13)$$

One can show that the minimization of this functional is equivalent to minimization of the parameter

$$\beta_A=\frac{\langle|\psi|^4\rangle}{\langle|\psi|^2\rangle^2}\ , \quad (14)$$

where the average is taken over the lattice primitive cell. The minimization of β_A as a function of α, ρ and k has

been performed numerically. The results of this minimization procedure shown in Figs. 7 and 8 appear to be in a good qualitative agreement with the experimental data. We observe the transformation of the lattice and increase of the vortex core anisotropy with the increase of the field. All the transformations are smooth and both vortex sizes depend on the field. In the low field limit (but still above H^*) the nonlinear term in the GL equations becomes significant and should be taken into account more accurately, i.e. beyond the approximation of a single Landau level adopted above.

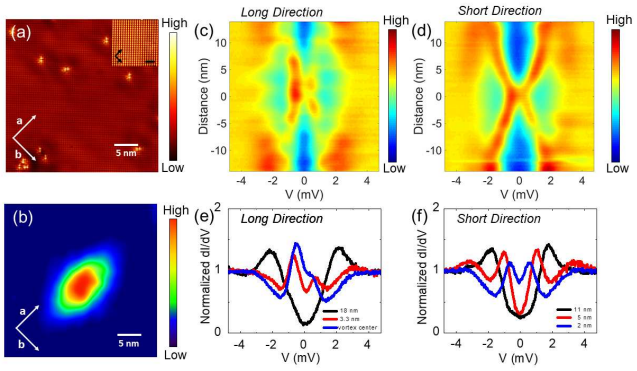

FIG. 1. (Color online) (a) A topographic STM atomic resolution image of size 31.9 nm x 31.9nm. Crystallographic axes a and b are presented at 45° from the topmost Se layer, representing the underlying Fe-Fe directions. The topography was acquired with V = 10mV, I = 100pA. The inset shows a zoom-in of the topmost Se lattice of size 10nm x 10nm. The scale bar in the inset is 2nm. (b) Differential conductance map at E=E_F and at H = 1.5T acquired simultaneously with the topography image in (a). The size of the image is 31.9 nm^2, and shows a single vortex. (c-d) Intensity plot obtained from a sequence of 160 spectra acquired along the long axis of the vortex core from the bottom left corner to the top right corner of the image in (b) (direction $\underline{a}$).(d) Intensity plot obtained from a sequence of 160 spectra acquired along the short axis of the vortex core from the left to the right of the image in (b) (direction $\underline{b}$). The spacing between the curves is 0.174 nm and the stabilization point for each curve is V= 5 mV, I= 60 pA for all curves in (c) and (d). (e) Characteristic tunneling spectra acquired along the direction $\underline{a}$ at the center of the vortex (blue) and at distances 3.3nm (red) and 18nm (black) from the vortex center.(f) Characteristic tunneling spectra acquired along the direction $\underline{b}$ at 2nm (blue), 5nm (red) and 11 nm (black) from the center of the vortex.

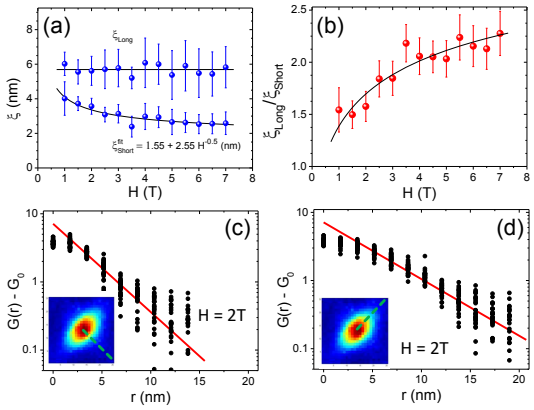

FIG. 2. (Color online) (a) ξ_{Long} and ξ_{Short} plotted as a function of applied magnetic field, dashed lines are guided for eyes. (b) Plot of ξ_{Long}/ξ_{Short} versus applied magnetic field, demonstrating an increase of the in-place anisotropy with increasing field. (c-d) The spatial dependence of zero-bias conductance away from a vortex core in two perpendicular directions. Its exponential decay fitted by $G(r) = G(0) + Ae^{-r/\xi}$ defines ξ_{Short} and ξ_{Long}, respectively.

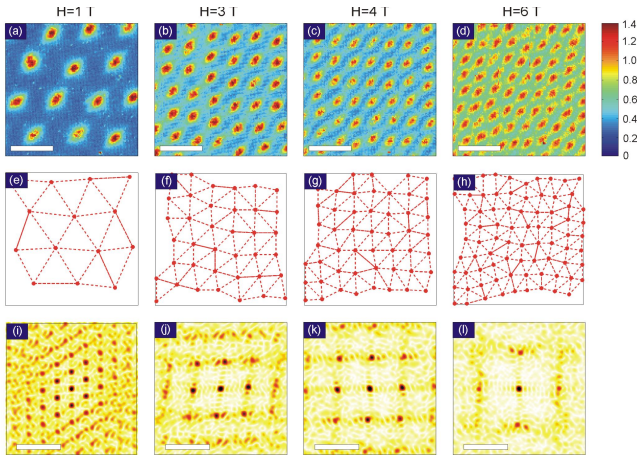

FIG. 3. (Color online)(a)-(d) Two-dimensional (2D) maps of the zero-bias conductance (ZBC), normalized to normal-state conductance at -10 mV, for the external magnetic field 1 T (a), 3 T (b), 4 T (c) and 6 T (d). These scanning tunneling spectroscopic measurements were carried out at 1.5 K over the area 156.2×156.2 nm^2 (the scale bar is 50 nm), during scanning process the height of the tip was controlled by a feedback loop and it corresponds to the current $I = 100$ pA at the bias $V = -20$ mV. (e)-(h) Two-dimensional (2D) Delaunay triangulation for the vortex patterns shown in the panels (a)-(d) for the same scanning areas, the filled red dots depict the positions of the vortex cores and red dash lines indicates the shortest distances between two neighbor vortices. (i)-(l) k-space (or 2D frequency domain) for the vortex lattices shown in the panels (e)-(h), respectively, obtained by a Fourier transformation (the scale bar is $0.04\mathring{A}^{-1}$. The vortex lattice at $H = 1$ T (a) is close to perfect hexagonal lattice; the vortex lattice at $H = 3$ T (b) can be described as a superposition of distorted hexagonal and square local lattices; the vortex lattice at $H = 4$ T (c) is close to perfect square lattice, while the vortex lattice at $H = 6$ T (d) becomes more blurred and it loses long-range-order.

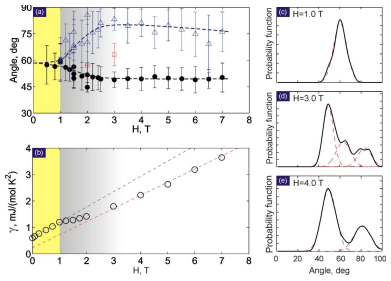

FIG. 4. (Color online) (a) Evolution of the inner angles between every three neighboring vortices, determined using with the Delaunay triangulation, as a function of the external magnetic field H. The error bars indicate the standard deviation; the dashed lines are guides to the eyes. The H range where the vortex lattice is close to hexagonal and all angles are close to 60° is shown in yellow; the H range corresponding to the transition from the hexagonal lattice to square lattice is shown in grey. (b) Dependence of the specific heat $\gamma(H)$ of the FeSe crystals on the external magnetic field H. The H range, where the transformation of the vortex lattice takes place (see panel (a)), correlates with the crossover from the linear dependence $\gamma(H) \propto H$ for low H-values to the linear dependence with different slope and offset for high H-values. (c)-(e) Typical probability distribution functions for the inner angles of the Delaunay triangles for $H = 1$ T (c), 3 T (d) and 4 T (e) and their Gaussian decomposition (red dash lines). There is a clear transition from the unimodal distribution with the single maximum near 60° (c), inherent for hexagonal lattice, to bimodal distribution with two local maxima near 45° and 80° (e), inherent for distorted square lattice. The probability distribution function with three maxima at 45°, 60° and 80° (d), observed in the transition region, point out to the co-existence of hexagonal and square lattices in the same scanning area. The peaks in probability distribution which corresponds to the hexagonal lattice are marked with red squares in (a).

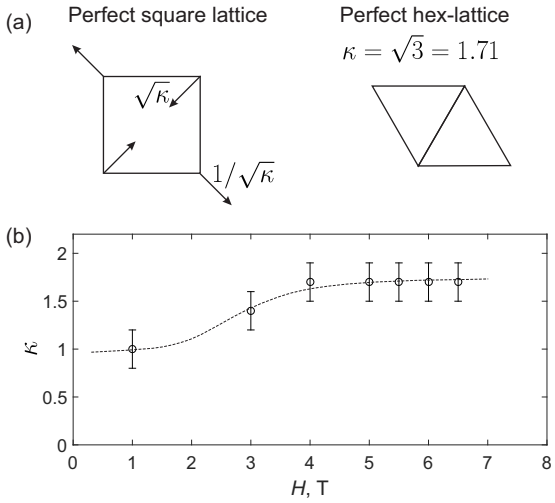

FIG. 5. (Color online) (a) We apply rescaling with the factor κ along the diagonals. For $\kappa = 1.71$ this rescaling transforms a square lattice into a hexagonal lattice. (b) Field dependence of the scaling ratio κ. The transformed lattice becomes hexagonal at $1T \leq H \leq 7T$ after applied transformation.

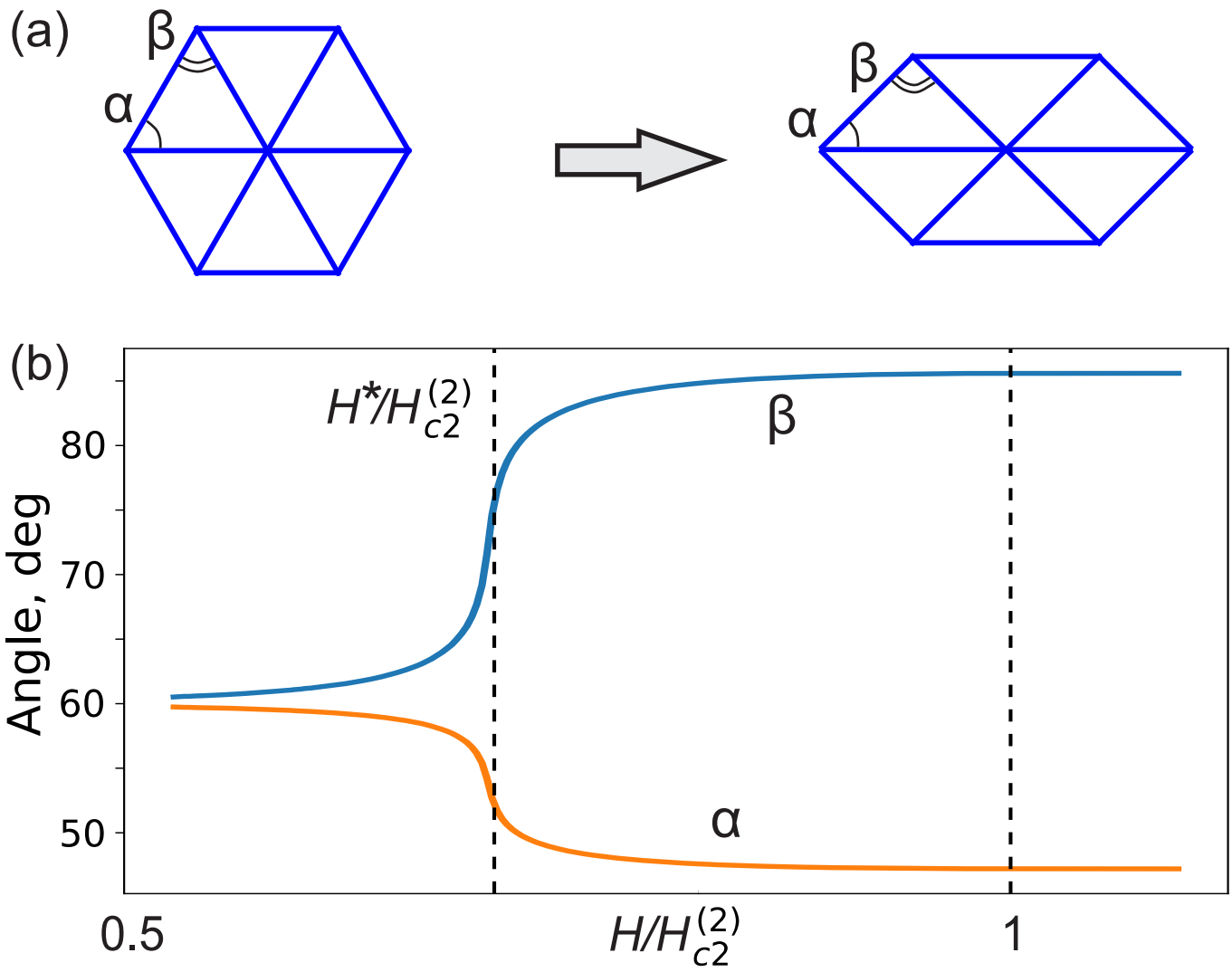

FIG. 6. (Color online) (a) Transformation from the hexagonal vortex lattice to the square one. The angles of the unit cell are denoted as α and β. (b) The angles of the unit cell of the vortex lattice vs. the magnetic field. The parameters are taken as follows: $\lambda^{(1)}/\xi^{(1)} = 34$, $\lambda^{(2)}/\xi^{(2)} = 3.5$, $\xi^{(2)}/\xi^{(1)} = 3$, $m_y^{(1)}/m_x^{(1)} = 3.5$ and $m_x^{(2)} = m_y^{(2)}$.

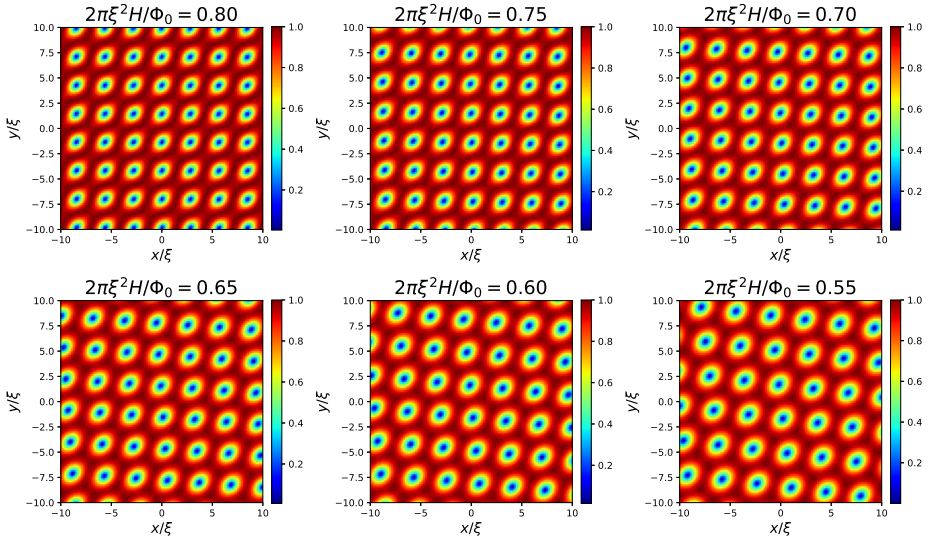

FIG. 7. (Color online) The order parameter profiles calculated for vortex lattices energetically favorable at different magnetic fields. The color indicates the absolute value of the order parameter ψ normalized onto its maximal value. The parameters of the non-local terms are $\mu_{xx} = 0.3$, $\mu_{yy} = 0.6$ and $\mu_{xy} = 0.6$. The vortex lattice smoothly transforms from the tetragonal one at high fields to the hexagonal at low fields.

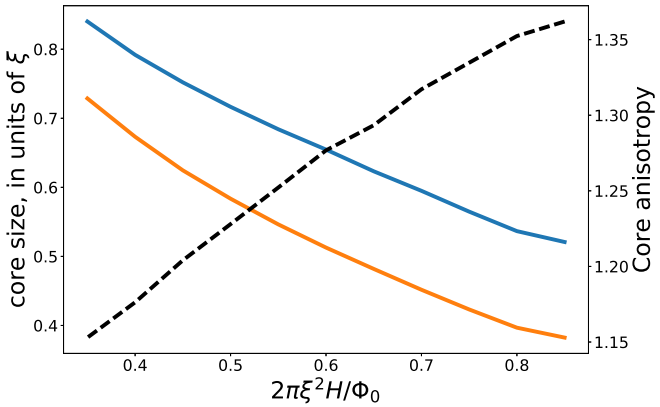

FIG. 8. (Color online) The core dimensions and their ratio vs the magnetic field.